Energy & Environmental Science

ROYAL SOCIETY OF CHEMISTRY

PAPER

View Article Online
View Journal | View Issue

Cite this: *Energy Environ. Sci.*, 2025, **18**, 9230

Capturing failure mechanisms toward the rational design of reversible vanadium oxide-based zinc batteries

Xuesong Xie, [a] Yang Yang, [a] Yifan Li, [a] Rohit Sinha, [a] Xuehai Tan, [a] Keren Jiang, [a] Minggang Xie, [a] Yuxuan Xue, [a] Ning Chen [b] and Zhi Li *[a]

Aqueous zinc ion batteries (ZIBs) have attracted increasing attention as alternative energy storage technologies due to their safety and low cost. However, the continuous dissolution of active materials in vanadium oxide-based ZIBs has posed an unavoidable challenge. Here, we systematically investigate the dissolution mechanism driven by chemical and electrochemical processes using both *ex situ* and *in situ* techniques. Experimental and theoretical analyses revealed an excessive reduction in the vanadium valency following H^+ insertion at potentials above 1.0 V (*vs.* Zn^{2+}/Zn), contributing to vanadium dissolution rather than Zn^{2+} insertion. Protons preferentially form monodentate coordination with oxygen, increasing local electron density around V atoms and facilitating 1s to higher-energy 3d electron transitions. This leads to a pronounced reduction in V-valency and V–O bond breakage. Specifically, interlayer-inserted H^+ exhibits the highest dissolution energy due to its significant binding energy compared to Zn^{2+} and surface-insertion. As a proof of concept, without additives or cathode modifications, improvements in Zn/$NH_4V_4O_{10}$ and Zn/V_2O_5 batteries were achieved by reducing the cut-off voltage or increasing the current density at high voltage to directly inhibit H^+ insertion or promote the favorable surface-dominant H^+ insertion. Further evidence is substituted by H^+-substituting cations (Na^+ and Li^+), which deliver sustained cycling stability at 0.2 A g^{-1} and extended cycling up to 5000 cycles at 5 A g^{-1} in both battery systems. We contend that understanding failure mechanisms is imperative for the development of strategies rooted in fundamental principles.

Received 28th June 2025,
Accepted 8th September 2025

DOI: 10.1039/d5ee03635f

rsc.li/ees

Broader context

With the growing emphasis on safety and sustainability, aqueous zinc-ion batteries (ZIBs) have garnered considerable attention as green and efficient energy storage alternatives. Despite significant progress in optimizing various battery components, vanadium oxide—one of the dominantly promising cathode materials—continues to suffer from uncontrolled and persistent dissolution, literally limiting its real-world implementation. In this work, we systematically demonstrate that excessive reduction of the vanadium valency, followed by the insertion and accumulation of layer-confined H^+ at high potentials, is the principal cause of vanadium dissolution. Guided by this mechanism exploration, rational strategies—such as lowering the cut-off voltage by directly inhibiting proton insertion, increasing current densities at high voltage that facilitate de-insertion of surface-inserted H^+, and introducing H^+-substituting cation electrolytes—were readily developed to achieve durable stabilization. We expect that this in-depth analysis will help address dissolution issues in related energy storage systems.

Introduction

Electrical energy storage is emerging as a pivotal strategy for transitioning from fossil fuels to environmentally sustainable resources. Nevertheless, organic battery technologies (*e.g.*, Li- and Na-based systems) are facing growing scrutiny, particularly concerning the risk of thermal runaway and environmental hazards associated with their utilization and recycling processes.[1,2] It becomes necessary therefore to prioritize green and environmentally sustainable alternatives for long-term demands. Recently, having achieved decent electrochemical performance with aqueous electrolytes,[3] ZIBs have been considered promising complementary candidates for meeting high safety and stability requirements because of their high specific capacity (820 mAh g^{-1}), benign electrochemical

[a] *Department of Chemical and Materials Engineering, University of Alberta, Edmonton T6G 1H9 AB, Canada. E-mail: zhi.li@ualberta.ca*
[b] *Hard X-Ray Micro Analysis BL, Canadian Light Source, Saskatoon, Saskatchewan S7N 2V3, Canada*

potential (−0.762 V *vs.* SHE), chemical inertness, and environmental friendness.[4,5] A growing body of literature has demonstrated the merits of ZIBs.[6] However, for aqueous electrolytes, the dissolution of active materials has consistently posed unavoidable and persistent challenges over extended periods.[7,8]

Vanadium oxide-based materials, as commonly used cathodes, have garnered considerable attention due to their multivalent redox chemistry and resource abundance,[9] particularly for high-mass-loading applications in practice (>15 mg cm^{-2}).[10,11] Although significant strides have been made, persistent dissolution problems continue to cause uncontrolled capacity decay and restricted calendar life, especially at current densities below 500 mA g^{-1} (Table S1). Notably, vanadium dissolution constitutes a fundamental challenge that transcends electrolyte formulations, occurring consistently across all conventional electrolyte systems ($ZnSO_4$, $Zn(CF_3SO_3)_2$, and $ZnCl_2$) with similar degradation.[12] Many efforts to mitigate dissolution include the protective cathode layer,[13,14] pre-insertion of metal ions and organic group,[15–17] adoption of ultra-high "water-in-salt" concentration electrolytes,[18–21] eutectic and gel electrolytes,[22–25] inorganic solid or colloidal electrolytes that we proposed,[26,27] and PAN or Nafion functional separator.[28,29] However, these result-oriented strategies primarily focus on morphological changes and electrochemical behavior arising from passive blocking and vanadium-valency reduction, while giving limited attention to quantitative analysis of intrinsic failure mechanisms.

Studies on the modification of V_2O_5 with intercalated polyaniline have reported that it stems from the attack on chemical V–O bonds following inserting cations. The strong polarization of Zn^{2+} weakens the V–O bonds and shifts them to a lower binding energy due to the competition between V–O and Zn–O bonds.[30] As evidence, various strategies, such as doping with heterogeneous ions or functional groups,[31] have been used to stabilize transfer channels and minimize local electric field concentration caused by Zn^{2+} de-insertion. Some studies have indicated that vanadium oxide undergoes a dominant proton intercalation along with the reversible precipitation of layer double hydroxide (LDH) in both $ZnSO_4/H_2O$ and $Zn(SO_3CF_3)_2/H_2O$ electrolytes.[32] Researchers Choi and Kim revealed that the main reason for the limited sustainability is caused by the electrochemically inactive zinc pyrovanadate phase gradually forming on the cathode surface.[33] Despite recent progress, the mechanistic understanding of vanadium dissolution in aqueous electrolytes remains limited, leading to ambiguity in strategy development.

Herein, we capture the dissolution mechanism of layered vanadium oxide-based ZIBs using $NH_4V_4O_{10}$ (NVO) and V_2O_5 (VO) cathodes at both the coin and cuvette system levels. As cycling continues in Zn/Zn batteries, the electrolyte pH increases dramatically from 4.4 to 5.4 within just 40 hours of the plating/stripping process at 1 mAh cm^{-2}. This increase in pH is accompanied by a gradual rise in vanadium content, which demonstrates vanadium chemical dissolution during the cycling procedure. Meanwhile, the electrochemically driven dissolution in V is confirmed by the excessive reduction of V valency during H^+ (de)insertion at higher voltage platforms, rather than by Zn^{2+} or hydrated species. Both processes result in the irreversible precipitation of vanadium-based zinc hydroxide, driven by continuous OH^- accumulation, and accelerate further dissolution, as illustrated in Fig. 1a. Theoretical calculations indicate that inserted protons with monodentate coordination tend to significantly reduce the V valency and induce V–O bond breakage. As proof, without any electrolyte additives or cathode modifications, electrochemical improvement in $Zn/NH_4V_4O_{10}$ and Zn/V_2O_5 batteries was achieved by simply reducing the cut-off voltage or increasing the current density at high voltage to directly inhibit H^+ insertion and mitigate the accumulation of layer-inserted H^+. This is attributed to the facile de-insertion of surface-inserted H^+ and its lower dissolution energy due to the weak binding energy (−0.82 eV) compared to Zn^{2+} (−3.6 eV) and the layer-inserted H^+ (−2.54 eV). Further evidence is substantiated by H^+-substituting cation (Na^+ and Li^+) electrolytes, which successfully suppress H^+-insertion around the 1.3 V platform with sustained cycling stability at 0.2 A g^{-1} and extended cycling up to 5000 cycles at 5 A g^{-1} in both battery systems. We believe that understanding the failure mechanism is critical to underscore the necessity of strategy development grounded in fundamental principles.

Results and discussion

To investigate the fading mechanism of the vanadium oxide-based ZIBs, the pH change of the electrolyte was first examined using an *in situ* pH monitor in the cuvette cell as schematically shown in Fig. S1. The electrodes (Zn/Zn) were placed in 2.5 mL of $ZnSO_4$ aqueous electrolyte (*vs.* 50 μL in the coin battery) with a pH monitor and then sealed. As shown in Fig. 1b, during galvanostatic cycling at a current density of 2 mA cm^{-2} and a specific capacity of 1 mAh cm^{-2}, the Zn deposition/stripping curve initially exhibits a voltage hysteresis of 55 mV and increases to 68 mV after just 40 cycles. After 3 hours of resting activation, the pH increases significantly from an initial value of 4.4 to 5.4 after cycling (Fig. 1c). Further investigation is warranted to elucidate the correlation between pH and vanadium dissolution. After artificially adjusting the pH value of the $ZnSO_4$ electrolytes, the pristine NVO cathodes were subsequently immersed in the solution. Inductively coupled plasma optical emission spectrometry (ICP-OES) results indicate that, at the same immersion time (24 h), an increase in pH corresponds to a greater concentration of V dissolution into the electrolyte (Fig. 1d). When the pH increases from pristine to 6.5, the concentration of dissolved vanadium rises from 0.01 to 0.05 mg L^{-1}. Interestingly, the concentration of Zn in the electrolyte decreases from 572 mg L^{-1} (pristine, pH = 4.0) to only 4.9 mg L^{-1} (pH = 6.5). This suggests that Zn ions in the electrolyte may precipitate as an irreversible phase hydroxylated zinc salt when the solution approaches near-neutral or alkaline conditions,[34] gradually depleting the active Zn^{2+}.

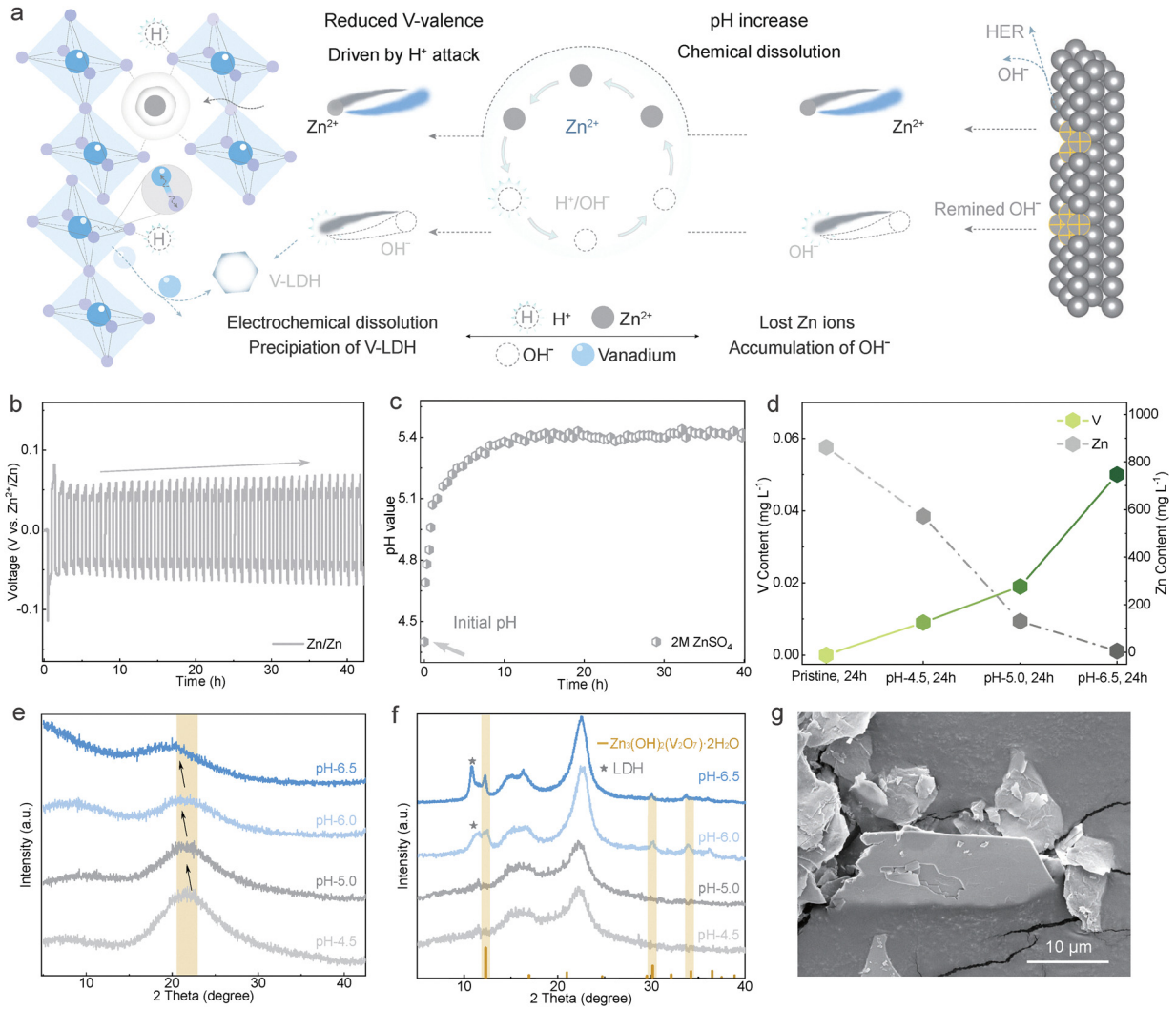

Fig. 1 Illustration of chemical changes and V dissolution demonstration. (a) Schematic illustration of the changes in Zn and V chemistry for vanadium oxide-based Zn batteries. (b) Charge–discharge curves of Zn/Zn batteries in a cuvette cell. (c) pH changes for a Zn/Zn battery cycled with 2 M $ZnSO_4$ at 2 mA cm^{-2}. (d) Changes in V and Zn content. (e) XRD patterns of the NVO electrode after immersing for 24 h. XRD patterns of electrolyte residual precipitation (f) and corresponding SEM image at pH 6.5 electrolyte (g).

After immersion, the NVO electrode in the pH 4.5 electrolyte exhibits an almost unchanged (110) diffraction peak at approximately 23° (Fig. 1e). As the pH increases to 5.0, the corresponding diffraction peaks of NVO electrodes are significantly weakened and gradually disappear under the same conditions in a pH 6.5 electrolyte. This suggests that severe chemical instability exists at elevated pH values, and the solubility trend is positively correlated with the increase in pH. Besides the layer double hydroxide precipitation of $Zn_3(SO_3)(SO_4)\cdot 3H_2O$ (LDH, PDF = 42-0096), the XRD results of the remaining deposits in the electrolyte indicate the formation of zinc hydroxide vanadium hydrate $Zn_3(OH)_2V_2O_7\cdot 2H_2O$ (V-LDH, PDF = 87-0417), with the increasing pH values (Fig. 1f). The SEM morphology presented in Fig. 1g, together with the distinct hexagonal shape identified in the elemental mapping of Zn, S, O, and V (Fig. S2), provides further evidence that the precipitate of V-LDH is formed through a deposition reaction of dissolved vanadium at an elevated pH of 6.5. During this process, active Zn^{2+} ions are simultaneously consumed. As a result, this precipitation subsequently accelerates the dissolution of vanadium into the electrolytes.

With different pH electrolytes, the electrochemical performances were evaluated in coin batteries. As shown in Fig. 2a, the charge/discharge curves demonstrate that the battery cycled with the baseline electrolyte (pH = 4.0) delivers a stable and high redox plateau at 1.1 V/1.0 V and 0.6 V/0.5 V. However, the platform gradually diminishes as the pH value increases from 4.5 to 6.0. Specifically, at a low current density of 0.2 A g^{-1}, similar results illustrate that the specific capacity of a Zn/NVO battery is inversely related to the electrolyte's pH value (Fig. 2b). The voltage hysteresis in the Zn/Zn symmetric battery further validated the deterioration as the pH increased (Fig. 2c). When cycled in an electrolyte with a pH of 6.0, the Zn/Zn symmetric battery sustains only 17 hours of repeated cycling at 1 mA cm^{-2}

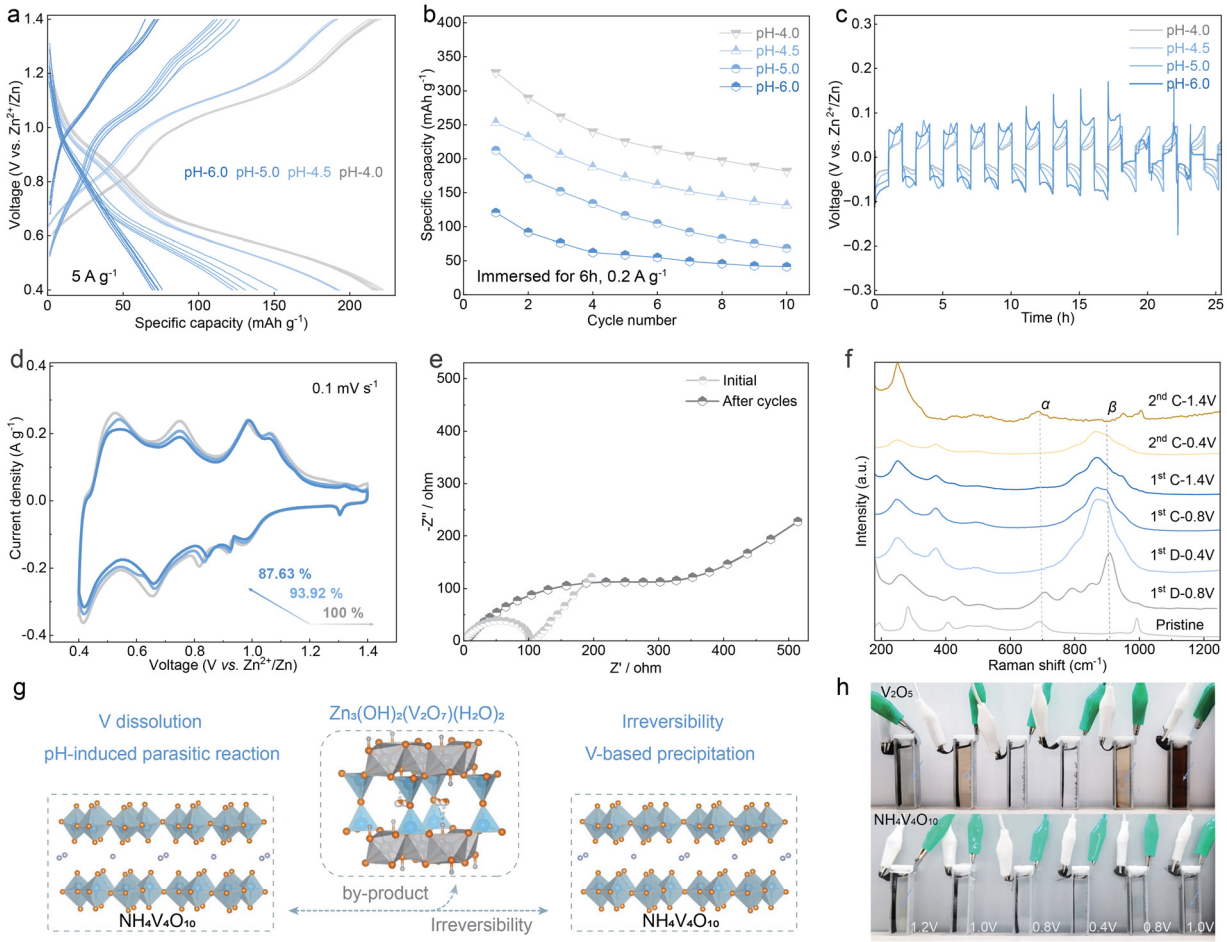

Fig. 2 Electrochemical performance under difference pH value electrolytes and V dissolution *in situ* characterization. (a) Charge–discharge curves of the Zn/NVO battery cycled at different pH values and (b) cycling performance at 0.2 A g^{-1}. (c) Zn plating/stripping behavior of the Zn/Zn battery. (d) CV curves of the Zn/NVO battery cycled with pristine electrolyte at a scan rate of 0.1 mV s^{-1}. (e) Nyquist plots of the Zn/NVO battery before and after cycling. (f) *Ex situ* Raman spectra of the Zn/NVO battery at a current density of 0.1 A g^{-1}. (g) Crystal structure changes along with V dissolution. (h) Photograph of V dissolution in the cuvette system.

(1 mAh cm^{-2}) and delivers the highest voltage hysteresis with an average of 170.5 mV compared to the baseline electrolyte (36.3 mV *vs.* Zn^{2+}/Zn). These results demonstrate that the attenuation of Zn/NVO is closely linked to the increasing pH value of the electrolyte.

In addition to chemical dissolution, electrochemically induced failure was also investigated. As shown in Fig. 2d, cyclic voltammetry (CV) analysis of Zn/NVO batteries, performed using a standard 2 M $ZnSO_4$ at a scan rate of 0.1 mV s^{-1}, shows only 87.63% capacity retention after three cycles. The improved capacity retention of 92.97% at a higher scan rate of 0.2 mV s^{-1} (99.97% at 0.5 mV s^{-1}) indicates enhanced reversibility with current density increase (Fig. S3), consistent with other vanadium oxide-based batteries at lower current densities, as listed in Table S1. Meanwhile, the dramatic increase in ionic transference resistance after cycling (291.6 Ω *vs.*77.9 Ω for a fresh electrode), as shown in Fig. 2e, indicates that severe side reactions occur to hinder ion transport, which is confirmed by the appearance of V-LDH precipitation in the XRD analysis (Fig. S4a). It strongly validates that both V dissolution and pH increase occur during electrochemical cycling with the baseline electrolyte. Specifically, *ex situ* Raman results further confirm the occurrence of a conversion reaction from an α-layer structure to a β-tunnel structure (Fig. 2f),[35] corresponding to the transition from the initial state to the end of discharge at 0.4 V (*vs.* Zn^{2+}/Zn). However, only a partial phase reverts to the initial state after charging to 1.4 V, implying an irreversible process during cycling (Fig. 2g). *Ex situ* XRD confirms that the diffraction signal of V-LDH appears at high voltage ranges during both the charge and discharge processes, and it gradually increases for cycling end of 1.4 V for both NVO- and VO-based batteries (Fig. S4b and S4c).

To accurately assess electrochemical dissolution, *in situ* operating models of Zn/NVO and Zn/VO batteries were implemented in a cuvette system. As shown in Fig. 2h and video 1, both Zn/NVO and Zn/VO batteries exhibit an obvious active dissolution at higher voltages (deep color above 1.0 V *vs.* Zn^{2+}/Zn), while no significant changes are observed in the lower voltage range. The ICP-OES and XRD results provide further confirmation of this tendency (Fig. S5a). Meanwhile, the

increase in pH values from 3.4 to 5.02 as batteries discharge from 1.4 V to 1.0 V (Fig. S6), along with the absence of Zn elements (Fig. S7a) in the EDS analysis at a discharge voltage of 1.0 V (*vs.* Zn^{2+}/Zn), highly indicates that the insertion process originates from proton or hydrated-proton at higher voltage range rather than Zn^{2+}. The remaining OH^- will either participate with the $ZnSO_4$ to form a LDH deposit (Fig. S7b), or with dissolved vanadium species to produce a V-LDH deposit on the cathode surface (Fig. S8a and b). As the discharge proceeds from 1.0 V to 0.4 V, in addition to Zn^{2+} insertion, substantial H_2 bubbles are observed at the anode from hydrogen reaction as shown in Fig. 2h, which further accelerates LDH deposition on the cathode surface, as confirmed by XRD and SEM results (Fig. S5b and S8c, d). The charging process undergoes the reverse reaction, beginning with Zn^{2+} extraction (0.4–1.0 V), followed by proton release from the cathode occurrent in V-LDH and LDH dissolution.

Based on the above analysis, *ex situ* and *in situ* X-ray absorption spectroscopy (XAS) using synchrotron radiation was further performed to quantitatively investigate the mechanisms and electrochemically induced structural transformations of the cathode in tape-type batteries (Fig. 3a). Regarding the X-ray absorption near edge structure (XANES) spectra of V K-edge (Fig. 3b), the experimental features properly matched the theoretical simulation used (Fig. S9a). After the first discharge to 1.0 V (*vs.* Zn^{2+}/Zn), the absorption edge of vanadium (V) shifts by around 1.32 eV toward lower photon energy compared to the initial electrode. Accordingly, the valence fitting performed on the V K-edge exhibits a significant reduction from the initial value of 3.42 to 2.58, as presented in Fig. 3c. Despite thorough washing of the electrodes before testing, the vanadium oxidation state may still be affected by residual precipitation of LDH and V-LDH phases, which can obscure the intrinsic valence evolution during cycling. Accordingly, theoretical calculations will be performed in the following analysis. The high intensity of the white line indicates an increased number of vacancies in the vanadium 3d states, thereby facilitating more electron transitions from 1s (core level) to a higher energy 3d.[36] This is primarily caused by the inserted ions, which weaken the electron compensation capability and the hybridization effect between the V–O bonds, leading to a tendency for bond breakage. As the discharge continues, the absorption edge of V nearly returns to its initial energy, starting from the discharge at 0.8 V and continuing until the end of the discharge at 0.4 V.

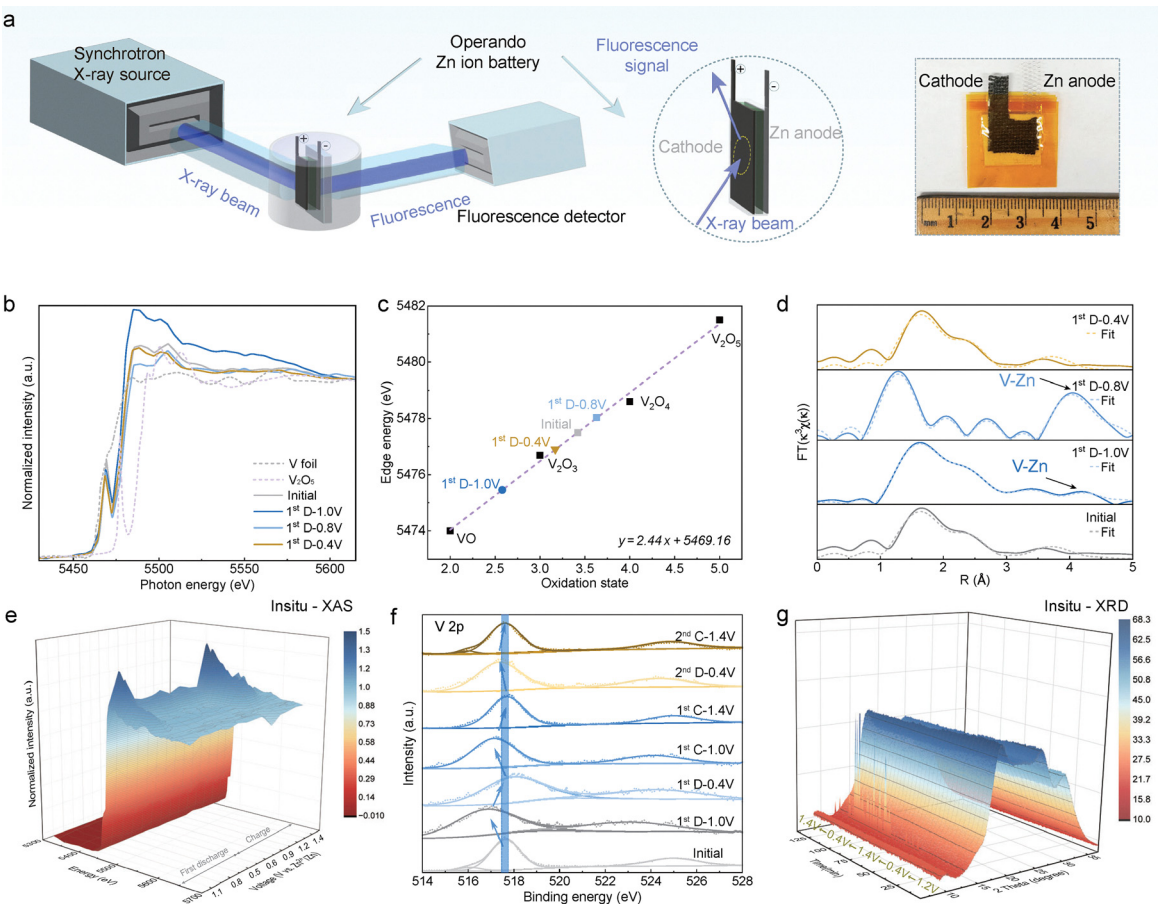

Fig. 3 *Ex/in situ* characterization based on tape-type batteries. (a) Schematic illustration of the *in situ* X-ray absorption spectroscopy (XAS) synchrotron radiation setup and the tap-type batteries. (b) Normalized XANES spectra of V K-edge for NVO after the first charge/discharge cycle, along with the corresponding fitted valence results (c), and k^3-weighted V K-edge FT-EXAFS spectra with fitting curves (d). (e) *In situ* XANES spectra of the first cycle based on tape-type Zn/NVO batteries. (f) *Ex situ* XPS. (g) *In situ* XRD characterization.

The detailed local coordination using Fourier-transformed X-ray absorption fine structure (FT-EXAFS), as shown in Fig. 3d, revealed a dominant peak at around 4.33 Å after reaching 0.8 V, strongly indicating the presence of V–Zn bonds during battery cycling from 1.0 V to 0.8 V (Table S2 and Fig. S9b). This validated that before 1.0 V, the insertion is mainly dominated by H^+, consistent with the above analysis, while the Zn^{2+} process initiates at 1.0 V. More precisely, *in situ* XAS was specifically designed to evaluate this reversibility and provide comprehensive insights over charge/discharge cycles. As shown in Fig. 3e, a dramatic fluctuation in the white line is evident in the V K-edge XANES spectra within the high voltage range (above 1.0 V) during both the charge and discharge process. This indicates a significant decrease in vanadium valence and an increase in the vacancies in the 3d orbitals due to H^+ (de)insertion at high voltage, which is primarily attributed to the irreversible dissolution reactions in NVO-based batteries.

Ex situ characterization studies of X-ray photoelectron spectroscopy (XPS) analysis also reveal a significant negative shift in V 2p peaks from 517.7 eV to 516.8 eV after discharging to 1.0 V, which highly indicates a pronounced reduction in the vanadium valence state following ion insertion at high voltage ranges compared to full discharge to 0.4 V,[37,38] as shown in Fig. 3f and Fig. S10a. This energy shift of V–O bonds to lower binding energy renders the vanadium oxide structure thermodynamically unstable due to the competition between H–O and V–O chemical bonds.[30] Hereafter, *in situ* XRD was investigated to analyze the resulting reactions in the tape Zn/NVO battery during the CV performance at a scan rate of 2 mV s^{-1}. As opposed to the repeated appear/disappear diffraction peak of the precipitation of V-LDH at around 12.3° degrees (Fig. 3g and Fig. S10b),[39] the gradually increasing peak demonstrates a continuous rise in pH and the persistence of V dissolution within the electrolyte environment. The progressive emergence of V-LDH signals, as revealed by the *in situ* XRD results during the second cycle (Fig. S10c), further confirms that its formation occurs in the high-voltage region (above 1.0 V) as discussed above.

Density functional theory analyses were performed to validate the differences after H^+ and Zn^{2+} insertions (Fig. S11). As illustrated in Fig. 4a, the interlayer-inserted proton preferentially forms a monodentate coordination with an oxygen atom, and exhibits a strong binding energy of −2.54 eV (Fig. 4b). In contrast, Zn^{2+} tends to build tetrahedral coordination, with a lower binding energy of −1.9 eV and an even electron distribution. All H^+ insertions result in a significant local electron concentration around V atoms in both layer and surface insertions. Owing to their smaller ionic radius and higher charge density, protons facilitate stronger electrostatic interactions toward the oxygen element and reduce the hybridization effect between the V–O bonds due to electron redistribution in the H–O–V local environment. The significantly longer bond length confirms the vulnerability and weakness of the V–O bonds (Table S3), which is correlated with the electron transition to higher energy levels as mentioned by XANES analysis. Eventually, proton insertion reduces the binding energy of V–O bonds, destabilizing the vanadium oxide structure.

In addition, the valence state of V_0 which is directly linked to proton insertion, undergoes a more significant decline compared to both the indirectly linked atoms (V_1, V_2, and V_3) and Zn^{2+} insertion at both layer and surface sites, as revealed *via* Bader charge analysis (Fig. 4c). Specifically, as for the surface-inserted H^+, the lowest binding energy (−0.82 eV) suggests that protons are more easily released from the surface compared to surface-inserted Zn^{2+} (−3.6 eV) and layer-inserted H^+. This is further validated by the higher coulombic efficiency of 99.78% when the current density increased to 1 A g^{-1} above 1.0 V (Mod, Fig. 4d), compared to the pristine efficiency of 97.6% at 0.2 A g^{-1} across the entire voltage range. This suggests that a higher current density improves capacity reversibility, mainly attributable to proton insertion occurring at the surface, which effectively mitigates further insertion and accumulation within the interlayered structure. This finding explains the widely documented correlation between elevated current densities and superior capacity retention.[40] Furthermore, the molecular dynamic (MD) simulation in $ZnSO_4$ electrolytes (Table S4) illustrated the association effects and dissolution trends under all types of ion insertion conditions. All types of Zn-insertion exhibit higher total energy compared to proton-insertion (Table S5), illustrating a reduced tendency for dissolution compared with proton insertion, which is consistent with the above analysis. When the number of inserted protons increases to two, the layer-inserted 2H shows an obvious dissolution (Fig. 4e), with the highest total energy of −16 375.24 eV and the largest coordination number of 10.0 in $ZnSO_4$ electrolytes. As established, capacity fading is primarily attributed to interlayer H^+ insertion at elevated voltage range and subsequent accumulation within the interlayered structure.

Consequently, the optimization strategy focuses on either reducing the accumulation of protons within the layered position or directly lowering the cut-off voltage. As a proof of concept, the current density was increased to 1 A g^{-1} when the voltage exceeded 1.0 V, which is five times higher than the 0.2 A g^{-1} applied as mentioned in Fig. 4d. The modification of voltage manifests superior stability retention of 82.61% compared to 64.60% for the pristine (Fig. 4f). Meanwhile, the enhanced stability was validated by gradually lowering the cut-off voltage (Fig. 4g). As the cut-off voltage decreased, capacity retention improved, albeit with a reduction in specific capacity, suggesting that protons also contribute to the overall capacity. Among them, the cut-off voltage of 1.2 V shows the best specific capacity and stability. This concept and strategy were further validated in Zn/V_2O_5 batteries, as shown in Fig. S12.

Further validation of the proton effect is achieved by 1 M Na_2SO_4 and 1 M Li_2SO_4 into the baseline electrolytes, thereby establishing a strategy based on H^+-substituting cations (Na^+ and Li^+). Based on the Gibbs free energy change and ion insertion calculations, the theoretical insertion potentials are determined to be 1.38 V and 1.1 V for Li^+, and 1.2 V for Na^+ (Fig. 5a and Fig. S13), indicating their potential to substitute for protons. The absence of Zn at voltages above 1.0 V, along with

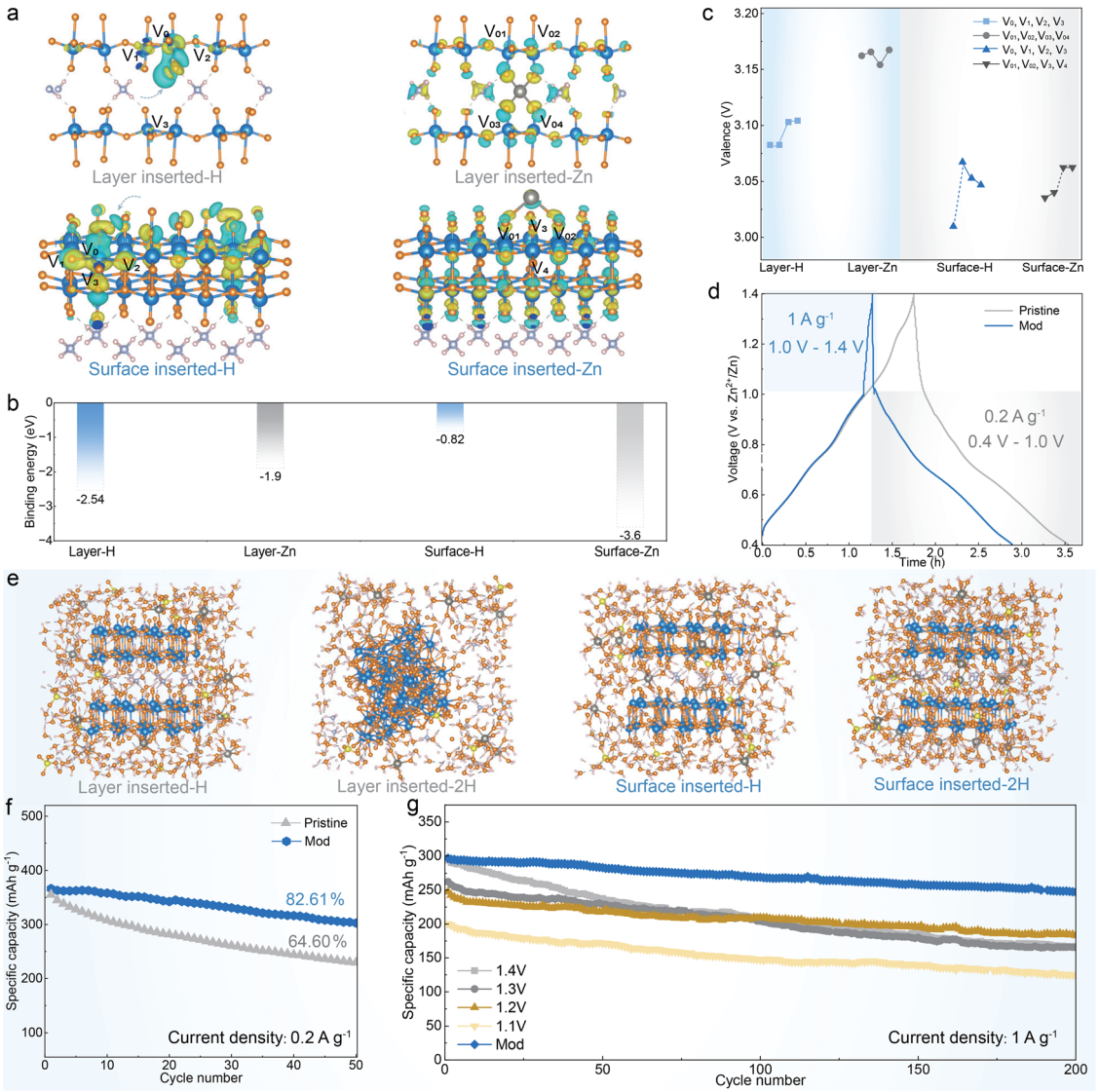

Fig. 4 Theoretical calculations and molecular dynamic simulation. (a) Electron density differences of NVO after layer and surface insertion of H^+ and Zn^{2+}, respectively. (b) Binding energy for ion insertions. (c) The valence state of vanadium atoms around the insertion site. (d) Galvanostatic and modified charge–discharge curves of Zn/NVO batteries. (e) MD simulation results of all types of proton insertion conditions in 2 M $ZnSO_4$ electrolytes. Cycling performance of batteries with different cut-off voltage and modification at 0.2 A g^{-1} (f) and 1 A g^{-1} (g), respectively.

the changes in peaks around 1.30 V observed in the CV results (Fig. 5b), indicates successful suppression of H^+ insertion in the Li-based electrolyte and elimination in the Na-based electrolyte. Meanwhile, the theoretical insertion voltage aligns with the CV peaks at around 0.8 V, 0.67 V, and 0.4 V, showing possible insertion positions of pure Zn^{2+} (Fig. S14a). With well-defined Zn element mapping (Fig. S8c) and the exclusion of pure Zn^{2+} insertion, the peaks at 1.0 V and 0.9 V can be attributed to the insertion of hydrated Zn^{2+}. This is further supported by theoretical calculations of hydrated Zn^{2+} coordinated with H_2O molecules (Fig. S14b). During the charging process, ion de-insertion shows sluggish kinetics, as evidenced by the large separation between redox peaks in the CV results. This accounts for the optimal specific capacity and reversibility achieved at the 1.2 V cut-off voltage as mentioned above. As a consequence, the NVO- and VO-batteries with H^+-substituting cation (Na^+, Li^+) electrolytes exhibit sustainable cycling stability across current densities from 0.2 A g^{-1} to 5 A g^{-1}, surpassing those with pristine electrolytes (Fig. 5c and S15). The batteries cycled with Li-based electrolytes deliver a higher specific capacity at the beginning of cycling but still exhibit gradual and consistent capacity fading, which may be due to only partial protons substitution, as indicated by the reduced peaks at 1.30/1.35 V and above. As for the Na-based electrolyte, the clearly identified Na element mapping from HRTEM-EDS results at the end of 1.0 V discharge indicates successful Na insertion (Fig. S16). Meanwhile, CV analysis confirms that it also effectively blocks proton or hydrated-proton insertion in subsequent cycles. As a result, it maintains 90% capacity retention for Zn/VO batteries after 200 cycles at 0.2 A^{-1} and nearly 100% retention for

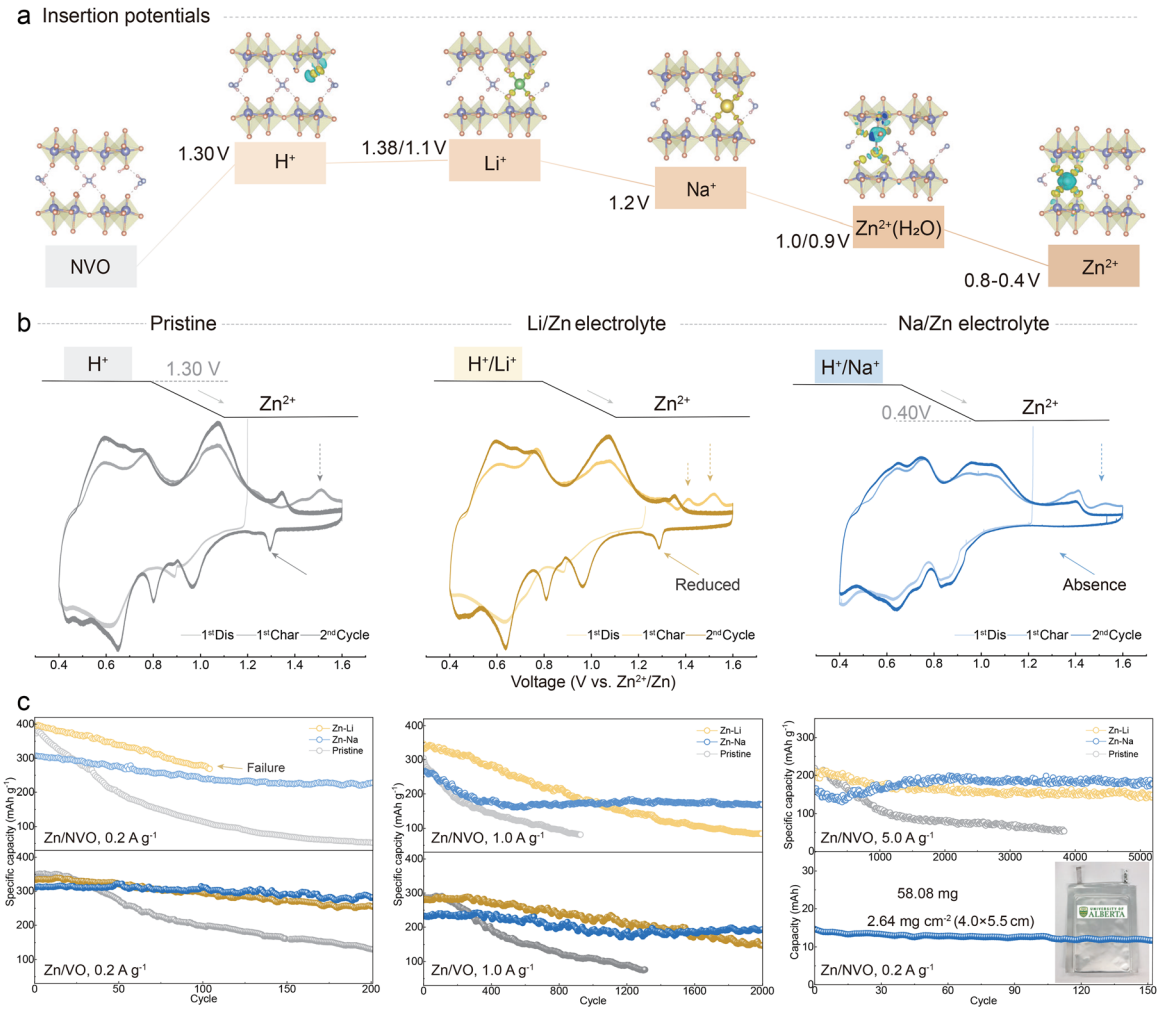

Fig. 5 (a) Electrochemical insertion potentials of ions into NVO cathodes. (b) CV curves of Zn/NVO battery cycled with baseline, Li/Zn, and Na/Zn electrolytes at a scan rate of 0.1 mV s^{-1}. (c) The corresponding cycling performance of NVO- and VO-based batteries, as well as the single-layer pouch-type Zn/NVO battery.

Zn/NVO batteries after 5000 cycles at 5 A g^{-1}. The stable cycling performance of the single-layer pouch-type Zn/NVO battery, delivering a capacity of 14.4 mAh at 0.2 A g^{-1}, strongly indicates the effective suppression of vanadium oxide degradation even under low current densities. The stable pH evolution during the initial discharge, particularly above 1.0 V, along with the reduced vanadium content in the electrolyte of Zn/NVO cuvette batteries cycled with Li^+- and Na^+-containing electrolytes (Fig. S17 and Table S7), further confirms the suppression of proton insertion and vanadium dissolution.

The mechanism of capacity fading in layered vanadium oxide batteries is due to a chain reaction. Firstly, during the discharge process, the decreasing valence of vanadium, driven by proton or hydrated-proton insertion at high voltages, leads to its dissolution. Subsequently, the dissolved vanadium then reacts with zinc ions, resulting in the precipitation of the vanadium-based zinc hydroxide salt as the pH increases, caused by proton insertion and continuous hydrogen evolution reaction (HER) at the zinc surface. Finally, combined with zinc consumption, the precipitation of dissolved vanadium is exacerbated in the next cycle by the presence of excess OH^-. Based on the above analysis, the mechanism-guided strategies should focus on (Fig. 6): (i) selecting benign working voltage to inhibit proton insertion; (ii) minimizing the particle size to promote surface-dominant proton insertions to minimize the accumulation of protons within the layered position; (iii) developing high-potential substitution ions or polymers such as PANI,[41] glutamic acid,[42] *p*-aminophenol,[43] to compensate for or replace proton insertion, thereby fundamentally suppressing electrochemical dissolution caused by protons; and (iv) establishing highly stable zinc metal anode interfaces and bulk phase alloys to suppress the HER and reduce chemical dissolution due to increased pH in the solution.[44,45] It is demonstrated that these VO_x oxides (VO_2, V_6O_{13}, V_2O_3, and V_2O_5) with tunnel structure will undergo phase transformation to layer structure after the first charge or short cycle.[46,47] Therefore, a fundamental understanding of the failure mechanisms in layered VO_x is imperative for guiding the design of other cathode materials.

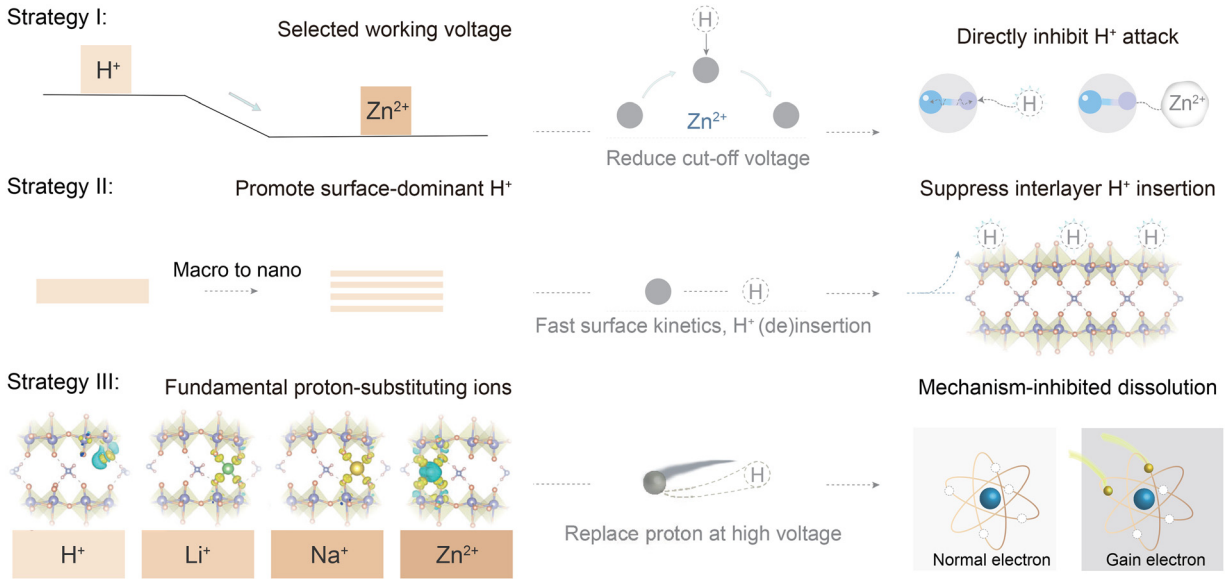

Fig. 6 Schematic illustration of mechanism-guided strategies for fundamentally mitigating vanadium dissolution toward reversible vanadium oxide-based zinc batteries.

Conclusions

In summary, we comprehensively analyze the vanadium dissolution in aqueous layered vanadium oxide-based ZIBs. It is recognized that the dissolution of vanadium is primarily attributed to the pronounced reduction in the vanadium valence state during proton insertion and subsequent accumulation within the layered structure at elevated voltages, rather than being driven by Zn^{2+}. Proton insertion preferentially forms monodentate coordination with oxygen, inducing intense localized electron concentration and subsequent V–O bond breakage. In contrast, Zn^{2+} tends to form a more uniform tetrahedral coordination, causing less disruption to the V–O bonds. As a chain reaction, the dissolved V precipitates with Zn^{2+} in the presence of remaining OH^- ions and is further exacerbated by the continuous generation of OH^- caused by the HER at the zinc anode and V-LDH deposition. As a proof of concept, without any additives or modifications of the cathode, the electrochemical improvement was achieved by simply reducing the cut-off voltage or increasing the current density at high voltage, which directly inhibited H^+ insertion or promoted surface-inserted reactions due to the lower binding energy of protons at the surface. Based on the revealed failure mechanism, the proposed H^+-substituting cation electrolytes (Na^+ and Li^+) demonstrate robust electrochemical stability at both 0.2 A g^{-1} and 5 A g^{-1} in coin and pouch systems. We believe that gaining insight into the thermodynamic properties of layered vanadium oxide-based electrodes and understanding the chemistry and electrochemistry-related failure mechanisms are crucial for their application.

Author contributions

X. X. designed the experiments and developed the concept. Y. Y. and Y. L. revised the manuscript. N. C. assisted with the XAS experiments and data analysis. Z. L. supervised the project. All authors discussed and commented on the manuscript.

Conflicts of interest

The authors declare no conflicts of interest.

Data availability

Supplementary information is available. See DOI: **https://doi.org/10.1039/d5ee03635f**.

Acknowledgements

This work was supported by the NSERC Alliance (ALLRP 571058-21) – Alberta Innovates Advance (212200888), NSERC Discovery Grant (RGPIN-2019-04660) program. The authors gratefully acknowledge the technical support provided by the nanoFAB at the University of Alberta. Support from the Hard X-ray Micro-Analysis Beamline (HXMA) team at the Canadian Light Source in acquiring and processing XAS data is also sincerely acknowledged.

References

1 L. Suo, O. Borodin, T. Gao, M. Olguin, J. Ho, X. Fan, C. Luo, C. Wang and K. Xu, *Science*, 2015, **350**, 938–943.
2 L. Ma, M. A. Schroeder, O. Borodin, T. P. Pollard, M. S. Ding, C. Wang and K. Xu, *Nat. Energy*, 2020, **5**, 743–749.
3 C. Xu, B. Li, H. Du and F. Kang, *Angew. Chem., Int. Ed.*, 2012, **51**, 933–935.
4 F. Wan, L. Zhang, X. Dai, X. Wang, Z. Niu and J. Chen, *Nat. Commun.*, 2018, **9**, 1656.

5 L. Wang, K.-W. Huang, J. Chen and J. Zheng, *Sci. Adv.*, 2019, **5**, 4279.
6 G. Li, L. Sun, S. Zhang, C. Zhang, H. Jin, K. Davey, G. Liang, S. Liu, J. Mao and Z. Guo, *Adv. Funct. Mater.*, 2024, **34**, 2301291.
7 Z. Pan, X. Liu, J. Yang, X. Li, Z. Liu, X. J. Loh and J. Wang, *Adv. Energy Mater.*, 2021, **11**, 2100608.
8 C. Liu, X. Xie, B. Lu, J. Zhou and S. Liang, *ACS Energy Lett.*, 2021, **6**, 1015–1033.
9 S. Liu, L. Kang, J. M. Kim, Y. T. Chun, J. Zhang and S. C. Jun, *Adv. Energy Mater.*, 2020, **10**, 2000477.
10 R. Ling, S. Zhao, C. Meng, W. Wang, C. Yang and W. Qi, *Small*, 2024, **20**, 2404089.
11 L. He, C. Lin, L. Zeng, F. Xiao, H. Lin, P. Xiong, Q. Qian, Q. Chen, Z. Yan and J. Chen, *Angew. Chem., Int. Ed.*, 2024, **64**, e202415221.
12 Z. Xing, G. Xu, J. Han, G. Chen, B. Lu, S. Liang and J. Zhou, *Trends Chem.*, 2023, **5**, 380–392.
13 D. Xu, H. Wang, F. Li, Z. Guan, R. Wang, B. He, Y. Gong and X. Hu, *Adv. Mater. Interfaces*, 2019, **6**, 1801506.
14 J. Guo, J. Ming, Y. Lei, W. Zhang, C. Xia, Y. Cui and H. N. Alshareef, *ACS Energy Lett.*, 2019, **4**, 2776–2781.
15 C. Xia, J. Guo, P. Li, X. Zhang and H. N. Alshareef, *Angew. Chem., Int. Ed.*, 2018, **57**, 3943–3948.
16 Y. Yang, Y. Tang, G. Fang, L. Shan, J. Guo, W. Zhang, C. Wang, L. Wang, J. Zhou and S. Liang, *Energy Environ. Sci.*, 2018, **11**, 3157–3162.
17 S. Chen, K. Li, K. S. Hui and J. Zhang, *Adv. Funct. Mater.*, 2020, **30**, 2003890.
18 F. Wang, O. Borodin, T. Gao, X. Fan, W. Sun, F. Han, A. Faraone, J. A. Dura, K. Xu and C. Wang, *Nat. Mater.*, 2018, **17**, 543–549.
19 L. Zhang, I. A. Rodríguez-Pérez, H. Jiang, C. Zhang, D. P. Leonard, Q. Guo, W. Wang, S. Han, L. Wang and X. Ji, *Adv. Funct. Mater.*, 2019, **29**, 1902653.
20 H. Jiang, L. Tang, Y. Fu, S. Wang, S. K. Sandstrom, A. M. Scida, G. Li, D. Hoang, J. J. Hong, N.-C. Chiu, K. C. Stylianou, W. F. Stickle, D. Wang, J. Li, P. A. Greaney, C. Fang and X. Ji, *Nat. Sustainability*, 2023, **6**, 806–815.
21 L. Zhang, Y. Han, Y. Geng, H. Zhang, H. Liu, Y. He, Z. Yan and Z. Zhu, *Angew. Chem., Int. Ed.*, 2025, **64**, e202500434.
22 H. Qiu, X. Du, J. Zhao, Y. Wang, J. Ju, Z. Chen, Z. Hu, D. Yan, X. Zhou and G. Cui, *Nat. Commun.*, 2019, **10**, 5374.
23 M. Han, J. Huang, X. Xie, T. C. Li, J. Huang, S. Liang, J. Zhou and H. J. Fan, *Adv. Funct. Mater.*, 2022, **32**, 2110957.
24 H. Qiu, R. Hu, X. Du, Z. Chen, J. Zhao, G. Lu, M. Jiang, Q. Kong, Y. Yan, J. Du, X. Zhou and G. Cui, *Angew. Chem., Int. Ed.*, 2022, **61**, e202113086.
25 B. Zhang, L. Qin, Y. Fang, Y. Chai, X. Xie, B. Lu, S. Liang and J. Zhou, *Sci. Bull.*, 2022, **67**, 955–962.
26 X. Xie, H. Fu, Y. Fang, B. Lu, J. Zhou and S. Liang, *Adv. Energy Mater.*, 2021, **12**, 2102393.
27 W. Zhang, M. Dong, K. Jiang, D. Yang, X. Tan, S. Zhai, R. Feng, N. Chen, G. King, H. Zhang, H. Zeng, H. Li, M. Antonietti and Z. Li, *Nat. Commun.*, 2022, **13**, 5348.
28 Y. Fang, X. Xie, B. Zhang, Y. Chai, B. Lu, M. Liu, J. Zhou and S. Liang, *Adv. Funct. Mater.*, 2021, **32**, 2109671.
29 B. Wu, Y. Wu, Z. Lu, J. Zhang, N. Han, Y. Wang, X.-M. Li, M. Lin and L. Zeng, *J. Mater. Chem. A*, 2021, **9**, 4734–4743.
30 R. Li, F. Xing, T. Li, H. Zhang, J. Yan, Q. Zheng and X. Li, *Energy Storage Mater.*, 2021, **38**, 590–598.
31 Y. Liu, C. Lu, Y. Yang, W. Chen, F. Ye, H. Dong, Y. Wu, R. Ma and L. Hu, *Adv. Mater.*, 2024, **36**, 2312982.
32 P. Oberholzer, E. Tervoort, A. Bouzid, A. Pasquarello and D. Kundu, *ACS Appl. Mater. Interfaces*, 2019, **11**, 674–682.
33 Y. Kim, Y. Park, M. Kim, J. Lee, K. J. Kim and J. W. Choi, *Nat. Commun.*, 2022, **13**, 2371.
34 B. Lee, H. R. Seo, H. R. Lee, C. S. Yoon, J. H. Kim, K. Y. Chung, B. W. Cho and S. H. Oh, *ChemSusChem*, 2016, **9**, 1–10.
35 R. Baddour-Hadjean, M. B. Smirnov, K. S. Smirnov, V. Y. Kazimirov, J. M. Gallardo-Amores, U. Amador, M. E. Arroyo-de Dompablo and J. P. Pereira-Ramos, *Inorg. Chem.*, 2012, **51**, 3194–3201.
36 D. H. Pearson, C. C. Ahn and B. Fultz, *Phys. Rev. B: Condens. Matter Mater. Phys.*, 1993, **47**, 8471–8478.
37 S. Zhang, L. Chen, D. Dong, Y. Kong, J. Zhang, J. Liu and Z. Liu, *ACS Appl. Mater. Interfaces*, 2022, **14**, 24415–24424.
38 Q. Wang, J. Wu, M. Wang, H. Yu, X. Qiu and W. Chen, *Adv. Sci.*, 2024, **11**, 2307872.
39 P. Wang, X. Xie, Z. Xing, X. Chen, G. Fang, B. Lu, J. Zhou, S. Liang and H. J. Fan, *Adv. Energy Mater.*, 2021, **11**, 2101158.
40 Y. Dai, C. Zhang, J. Li, X. Gao, P. Hu, C. Ye, H. He, J. Zhu, W. Zhang, R. Chen, W. Zong, F. Guo, I. P. Parkin, D. J. L. Brett, P. R. Shearing, L. Mai and G. He, *Adv. Mater.*, 2024, **36**, 2310645.
41 S. Liu, H. Zhu, B. Zhang, G. Li, H. Zhu, Y. Ren, H. Geng, Y. Yang, Q. Liu and C. C. Li, *Adv. Mater.*, 2020, **32**, 2001113.
42 P. Zhang, Y. Gong, S. Fan, Z. Luo, J. Hu, C. Peng, Q. Zhang, Y. Li and X. Ren, *Adv. Energy Mater.*, 2024, **14**, 2401493.
43 Z. Song, Y. Zhao, A. Zhou, H. Wang, X. Jin, Y. Huang, L. Li, F. Wu and R. Chen, *Small*, 2024, **20**, 2305030.
44 Z. Cai, J. Wang and Y. Sun, *eScience*, 2023, **3**, 100093.
45 W. Xin, J. Xiao, J. Li, L. Zhang, H. Peng, Z. Yan and Z. Zhu, *Energy Storage Mater.*, 2023, **56**, 76–86.
46 W. Deng, C. Li, W. Zou, Y. Xu, Y. Chen and R. Li, *Small*, 2024, **20**, 2309527.
47 L. e Mo, Y. Huang, Y. Wang, T. Wei, X. Zhang, H. Zhang, Y. Ren, D. Ji, Z. Li and L. Hu, *ACS Nano*, 2024, **18**, 1172–1180.